

Scalable Oxygen-Ion Transport Kinetics in Metal-Oxide Films: Impact of Thermally Induced Lattice Compaction in Acceptor Doped Ceria Films

Jennifer L. M. Rupp,* Emiliana Fabbri, Dario Marrocchelli, Jeong-Woo Han, Di Chen, Enrico Traversa, Harry L. Tuller, and Bilge Yildiz

In this paper, we focus on the effect of processing-dependent lattice strain on oxygen ion conductivity in ceria based solid electrolyte thin films. This is of importance for technological applications, such as micro-SOFCs, microbatteries, and resistive RAM memories. The oxygen ion conductivity can be significantly modified by control of lattice strain, to an extent comparable to the effect of doping bulk ceria with cations of different diameters. The interplay of dopant radii, lattice strain, microstrain, anion-cation near order and oxygen ion transport is analyzed experimentally and interpreted with computational results. Key findings include that films annealed at 600 °C exhibit lattice parameters close to those of their bulk counterparts. With increasing anneal temperature, however, the films exhibited substantial compaction with lattice parameters decreasing by as much as nearly 2% (viz, $\Delta d_{600-1100\text{ °C}}$: -1.7% (Sc⁺³) > -1.5% (Gd⁺³) > -1.2% (La⁺³)) for the annealing temperature range of 600–1100 °C. Remarkably 2/3rd of the lattice parameter change obtained in bulk ceria upon changing the acceptor diameter from the smaller Sc to larger La, can be reproduced by post annealing a film with fixed dopant diameter. While the impact of lattice compaction on defect association/ordering cannot be entirely excluded, DFT computation revealed that the main effect appears to result in an increase in migration energy and consequent drop in ionic conductivity. As a consequence, it is clear that annealing procedures should be held to a minimum to maintain the optimum level of oxygen ion conductivity for energy-related applications. Results reveal also the importance to understand the role of electrochemo-mechanical coupling that is active in thin film materials.

1. Introduction

Decreasing the dimensions of ionic conductors to the nanoscale has enabled the realization of new electrochemical devices integrated on Si-based and other microsystems. These comprise fast ionic conducting electrolytes for energy-applications such as micro-fuel cells^[1,2] and batteries,^[3] gas conversion/reformation catalysts,^[4,5] sensors,^[6] and for redox-reaction based resistive memories.^[7,8] A key objective for these devices is to simultaneously achieve high device density per chip together with enhanced reaction and transport kinetics. Among various mixed ionic and electronic conducting (MIEC) oxides, doped ceria nano-scale films are of interest for a broad set of these microsystem based applications.^[6,9,10] Composition-defect and crystal structure-property correlations in bulk ceria-based solid oxide electrolytes are reasonably well established.^[11] Because of the low temperature processing conditions that are commonly required to insure proper integration with silicon and related technologies, the relations known for bulk ceria do not hold for nano-scale thin films.^[12]

Prof. J. L. M. Rupp, Dr. D. Marrocchelli, D. Chen,
Prof. H. L. Tuller

Department of Materials Science and Engineering
Massachusetts Institute of Technology
Cambridge, MA, 02139, USA

Prof. J. L. M. Rupp, Dr. D. Marrocchelli, Prof. J.-W. Han,
Prof. B. Yildiz

Department of Nuclear Science and Engineering
Massachusetts Institute of Technology
Cambridge, MA, 02139, USA

Dr. E. Fabbri
National Institute of Material Science (NIMS)
MANA, Tsukuba, Ibaraki, Japan

Dr. D. Marrocchelli
School of Chemistry
Trinity College Dublin
Dublin 2, Ireland

Prof. H. L. Tuller
International Institute for Carbon Neutral
Energy Research (WPI-I2CNER)
Kyushu University
Nishi-ku Fukuoka, 819-0395, Japan

Prof. J. L. M. Rupp
Department of Materials Science
ETH Zurich, Schafmattstr 30, 8093, Switzerland
E-mail: jennifer.rupp@mat.ethz.ch

Prof. E. Traversa
International Research Center for Renewable Energy
State Key Laboratory of Multiphase Flow in Power Engineering
Xi'an Jiaotong University
Xi'an, Shaanxi, 710049, China



DOI: 10.1002/adfm.201302117

And thus, a need exists to establish the composition-defect and crystal structure-property correlations, as well, in thin films. In this introduction, we first review the known relations of lattice parameter, ion radius and conduction properties of bulk ceria, and then discuss how thin films deviate from these relations.

1.1. What Is Known for Bulk Ceria?

Bulk ceria has been thoroughly characterized experimentally^[11,13,14] and computationally.^[15–21] One of the key desirable properties of ceria, for example, when used in solid oxide fuel cells (SOFCs), is its relatively high ionic conductivity and, therefore, much effort has been directed towards optimizing this quantity. The main strategy for enhancing the ionic conductivity has been to dope ceria with lower-valent cations of various sizes (usually tri-valent rare-earths or Ca^{2+}).^[11,22,23] The addition of trivalent cations leads, to the formation of oxygen vacancies to maintain charge neutrality, with the relation of $2[\text{V}^{\bullet\bullet}_{\text{O}}] = [\text{M}'_{\text{Ce}}]$, leading to increases in the oxygen ion diffusion coefficient through vacancies and, thereby conductivity. At the same time, each dopant alters the local defect configuration and thereby the ion migration barriers.^[15] The maximum value of the ionic conductivity of doped ceria therefore depends on both the dopant type and concentration.

As a general rule, dopants with radii similar to or slightly larger than that of Ce^{4+} , such as Sm^{3+} and Gd^{3+} , offer optimum oxygen ion conductivity, with the maximum conductivity in ceria achieved at approximately 20% dopant substitution.^[11,17] The addition of lower-valent cations affects the crystal structure of ceria, at both the local and the long-range levels. Indeed, the lattice parameter of these materials changes linearly with dopant cation concentration (and/or radius), in accord with Vegard's law.^[11,14,15] Due to the high sintering temperatures (usually ≈ 1500 °C), the lattice parameter is found to be processing independent within the range of bulk pellet processing conditions.^[11,13] At the local level, doping usually leads to association effects, that is, the preference for an oxygen vacancy to reside next to a specific cation, usually the one with the smaller radius. This is usually accompanied by local distortions of the lattice around the dopant cation and/or the oxygen vacancies.^[15] Recent work by Kossoy and Lubomirsky,^[24] for example, found that, for high Gd concentration ($>25\%$), ceria undergoes a transition to a double-fluorite phase where oxygen vacancies reside preferentially around the Ce cation. Similarly, for $\text{ZrO}_2\text{--CeO}_2$ solid solutions, oxygen vacancies reside preferentially around the smaller Zr ion which prefers the lower six-fold coordination.^[25]

Of interest is the manner in which the combined changes in composition (increased number of vacancies) and defect structure (association effects) impact the thermally activated ionic conductivity given by:

$$\sigma = \sigma_0 \exp(-E_a/k_B T), \quad (1)$$

where the pre-exponential factor, σ_0 , is proportional to the number of vacancies, $[\text{V}^{\bullet\bullet}_{\text{O}}]$. E_a , the effective activation energy, is typically treated by considering the effects of the migration enthalpy, ΔH_m and defect association enthalpy, ΔH_a , as:^[26]

$$E_a = \Delta H_m + \Delta H_a \quad (2)$$

While increasing the number of vacancies increases the conductivity (by a higher σ_0), the increase in association enthalpy reduces it. Numerous computational studies (often backed by experimental work) have focused on defect association effects. Early work by Minervini et al. has pointed to the importance of cation-vacancy association, by studying cation-vacancy dimers and trimers, and showed that vacancies prefer to reside next to the smaller cation.^[19,20] This trend was then confirmed by density functional theory calculations.^[19,21] More recent work has also pointed out the importance of the interaction and association of a vacancy with another vacancy^[16,27,28] and shown that these significantly affect the ionic conductivity of doped ceria. Cormack and co-workers have recently studied large-scale defect clusters and nano-domains,^[17,18] a more realistic picture than the simple dimers and trimers mentioned above. They found that sub-nanoscale defect clusters (prevalent at low dopant concentration) prefer a pyrochlore-type crystal structure in which dopants and vacancies are at next-nearest-neighbor sites. As these defect clusters grow into nanoscaled domains (typical of higher dopant concentrations), the C-type rare earth crystal structure, in which the dopants and vacancies are at nearest-neighbor sites, becomes more stable. This observation of C-type nano-scale domains is consistent with observations from TEM and SAED experiments.^[29–31] Interestingly, these different types of ordered domains also have slightly different lattice parameters, implying that defect association also affects the structural properties of these materials. Aside the impact of dopants on defect association energy, other studies have found corresponding effects of varying the dopant type and concentration on the migration enthalpy of the oxygen vacancies.^[32–35] We return to a consideration of the relative contribution of these two factors on ionic conduction in doped ceria films in the discussion section.

1.2. What Is Not Known for Thin Films?

Moving from bulk materials to thin films introduces new parameters that impact the crystal and defect structure as well as the transport properties. The functional characteristics of metal oxide thin films, such as crystal structure, phase, non-stoichiometry, concentration and mobility of charge carriers, often strongly depend on the deposition conditions established during processing (i.e., pO_2 , temperature, thermal history).^[36,37] Thin film microstructures range from dense to porous and differ in density, degree of crystallinity and strain.^[37–39] For example, a wide variation in the activation energy of oxygen ion conductivity (from 0.6 to 1.3 eV), dependent on the thin film processing history, was reported for Gd doped ceria (GDC), see review in the literature.^[40] This is in contrast to large-grain bulk GDC sintered pellets, which exhibit an activation energy of $E_a = 0.7$ eV, independent of processing route.^[11] The variable transport properties, observed in conducting oxide nano-films, represent a challenge in consistently controlling the performance of energy conversion or electronic-based microdevices with optimum and reproducible properties. We observe that the deviation of the thin film properties from those established in bulk ceria can arise from the presence of metastable phases (discussed below) resulting from the low-temperature synthesis

of the thin films, as well as from the strains that the films sustain. The latter is either in the form of “epitaxial strain” that represents the coherent lattice mismatch between the film and the substrate, or in the form of “microstrain” representative of the lattice disorder in the system. While the epitaxial strain is effectively a planar lattice expansion or compression in the film, the microstrain is measured in terms of the deviation of the lattice parameter from the average lattice parameter of the film, as reflected in the width of the peaks of an XRD pattern.

First we summarize the presence and consequences of metastable crystalline structures. Conventional semiconductor processes require temperatures below 700 °C to prevent the formation of silicon sub-oxides and assure compatible lithography routes.^[41,42] To be Si-technology compatible, metal oxide films are deposited at approximately one fifth of the melting temperature (conventionally <800 °C,^[43] or even lower, in contrast to the sintering of ceramic powders carried out at approximately two thirds of the melting temperature (>1400 °C). As a consequence of achieving equilibrium conditions during sintering, the lattice constants of bulk ceramics are found to be processing-independent.^[13,44] On the other hand, because of the relatively low synthesis temperatures, metastable microstructures, that differ substantially from those found in bulk sintered ceramics, tend to prevail in such films.^[40,45–48] The effective lattice parameter and the extent of disorder in thin films can vary significantly as a function of processing conditions.^[48–53] For example, instead of a fixed lattice constant for a given composition, irrespective of processing conditions, one finds evidence for processing-dependent lattice constants, and corresponding variations in the electrical and transport properties of thin oxide films as reported for nano-ceria^[39,45] and nano-zirconia^[49,50,54,55] films. Consequently, the conductivity-crystal structure relationships for thin film nanostructured materials is far less understood compared to those in bulk oxides. For micro fuel cells or sensors, the “operation” and “deposition” temperatures are close or even overlapping, adding further to the complications related to crystal and defect structure-property relations.^[42,53,56,57]

Second, we highlight the recent findings on the potential role of lattice strain in accelerating transport kinetics in solid state ionic and mixed ionic-electronic conductors (MIEC). The sensitivity of oxide properties to strain and defects is greatly amplified at interfaces, resulting in significant and quantifiable effects on charge-carrier density and mobility. Recent computational, analytical and experimental studies suggested a significant impact of lattice strain, in thin film zirconia, ceria and other systems, on facilitating oxygen ion transport.^[58–62] Additionally, other key properties of these materials, such as vacancy formation,^[63–68] are also facilitated. It is important to emphasize, however, that there is large scatter in the quantitative results for oxygen diffusion obtained experimentally in strained thin films or multilayers. For example, reported oxygen diffusivity enhancement ranges from a phenomenal $\times 10^8$ in ultra-thin YSZ films sandwiched between SrTiO₃ layers,^[58] to $\times 10^3$ in YSZ thin films on MgO,^[69] to a mild $\times 2$ in YSZ/Y₂O₃ multilayers,^[70] and nearly no change for YSZ/CeO₂ multilayers.^[71] Pennycook concluded from first principle calculations that the origin of colossal ionic conduction is mainly an extreme disordering of the oxygen sublattice, due, potentially, to the presence of an interface with SrTiO₃ and/or the lattice strain.^[72]

However, we take Pennycook’s predicted magnitude of improvement in ion transport with caution. Recent DFT calculations point to a reduced migration energy barrier for oxygen diffusion when the material is tensile strained, but a much more moderate improvement in ion conduction is expected at 700 K or above due to lattice strain alone, as detailed in the literature.^[73–76] Very recently, De Souza and co-workers extended current DFT models by analysis of the activation volume tensor to describe the impact of arbitrary strain states on oxygen ion migration energies, first implemented on ceria materials.^[77] From an experimental perspective the large scatter and lack of reproducibility arises,^[78,79] at least in part, from the processing dependent differences in film microstructure, strain state and chemistry. Processing-dependent lattice constants, associated with the fabrication of metastable or epitaxially strained thin films has an impact on the intrinsic chemical and transport properties of the material; an example of what is becoming popularly known as “electro-chemo-mechanics”.^[24,35,80] This area of investigation concerns itself with how changes in the mechanical/structural properties of materials (e.g., strain, lattice parameter) impact their electrical (e.g., ionic conductivity) and chemical (e.g., oxygen nonstoichiometry) properties and vice-versa. Control of lattice strain, for example, is being examined as an important strategy for modifying charge and mass transport kinetics in devices based on MIEC films,^[79] an approach common in the semiconductor industry, for example, to achieve enhanced electron mobilities.^[81]

The objective of this paper is to quantitatively and mechanistically assess the impact of the changes in the lattice parameter and microstrain on ionic conductivity in doped-ceria nanostructured films. Unlike traditional means for varying lattice parameter by doping, we demonstrate in this study that equivalently large changes in lattice parameter can be obtained, in a film of fixed composition, by control of the thermal history of the film. In this study, nanostructured films, prepared by pulsed laser deposition (PLD) at room temperature, exhibiting different strain levels (both lattice parameter and microstrain), are accessed through changes in post-annealing treatments. Studies are limited to compositions for which doped ceria remains single phase fluorite, (see **Figure 1a**), within which the ionic conductive character is controllable through doping with trivalent cations. La, Gd, Lu, or Sc were chosen as the dopants in this work, see **Table 1**. Since the dopant concentration is maintained constant at 20 mol% for each composition, the influence of the trivalent cation size on the thin film atomic structure can directly be assessed. In particular, lattice strain, microstrain and oxygen-cation distances were studied for each composition as a function of thermal history. The lattice parameters, lattice disorder and relative changes in the oxygen-cation bond distances were investigated with X-ray diffraction (XRD) and Raman spectroscopy. In particular the Raman spectroscopy is a powerful probe of local bond distances, which are inversely proportional to cation-oxygen bond strengths for ceria, an important parameter influencing ion migration energies.^[82,83] Oxygen ion transport was studied by electrochemical impedance spectroscopy. The effect of strain on the migration barrier and on defect association energy is assessed computationally using density functional theory calculations, and discussed in relation to the observed changes in ionic transport in

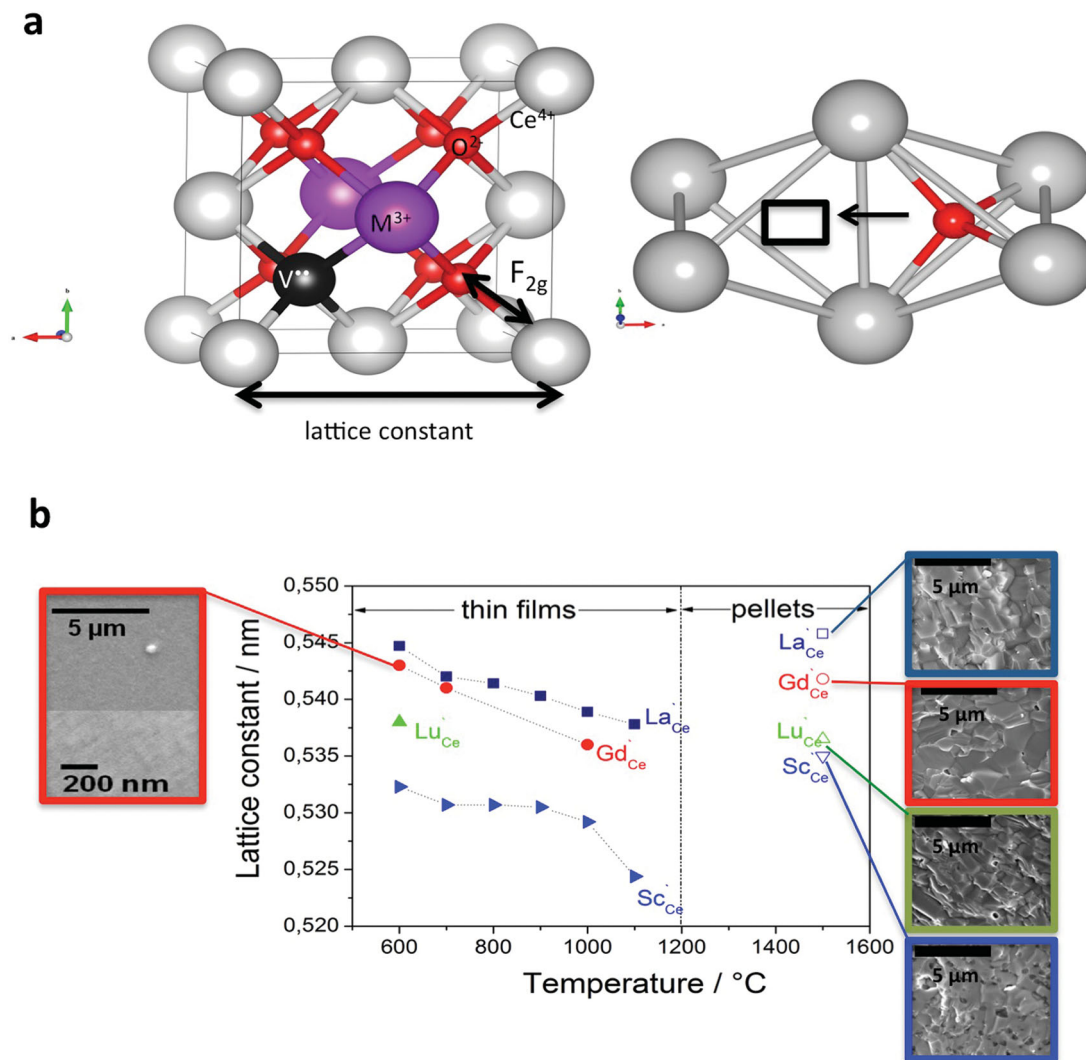


Figure 1. Lattice strain in binary oxide thin films. a) Fluorite ceria crystal structure indicated are the structural positions of oxygen ions (O^{2-}), ceria cations (Ce^{4+}), dopant cation (M^{3+}), oxygen vacancy ($V_{..}$), the lattice constant and the near order oxygen ion-cation F_{2g} bonds (left). The transport of oxygen ions through hopping over oxygen vacancies is indicated in its structural plane (right). b) Lattice constant of 20 mol% Sc, Lu, Gd and La-doped ceria thin films and sintered pellets with respect to post-annealing temperature of thin films and sintering temperature for pellets. Micrographs display exemplarily the SEM microstructures of pellets and thin film.

the thin films. Finally, implications for applications of strain-charge transport relations in ceria-based thin films, in miniaturized microsystem-based electrochemical devices, are discussed.

Table 1. Shannon ionic radii of host and dopant cations.^[133]

Cation	Ionic radius [pm]	Coordination	
Ce^{3+}	114	XIII	host lattice
Ce^{4+}	97	XIII	
La^{3+}	116	XIII	
Gd^{3+}	105	XIII	dopant
Lu^{3+}	98	XIII	
Sc^{3+}	87	XIII	

2. Results

Lattice constants were determined from XRD data on pellets and on fully crystalline thin films with different post-growth annealing temperatures. The lattice constant of the sintered bulk *pellets* increases with increasing radii of the solute cation from 0.535 nm (Sc^{3+}) to 0.546 nm (La^{3+}), Figure 1b (open symbols), and does not depend on processing conditions. The larger the dopant cation, the lower is the packing density of the ceria lattice. This finding is in agreement with previous experimental studies^[11,13] and computational work.^[84] The metastable nature of the thin films prepared in this study, on the other hand, is reflected in two distinct ways: 1) the lattice constant decreases significantly with increasing post-anneal temperature for each dopant, as displayed in Figure 1b, where the measured values for the highest post-annealing temperature are significantly

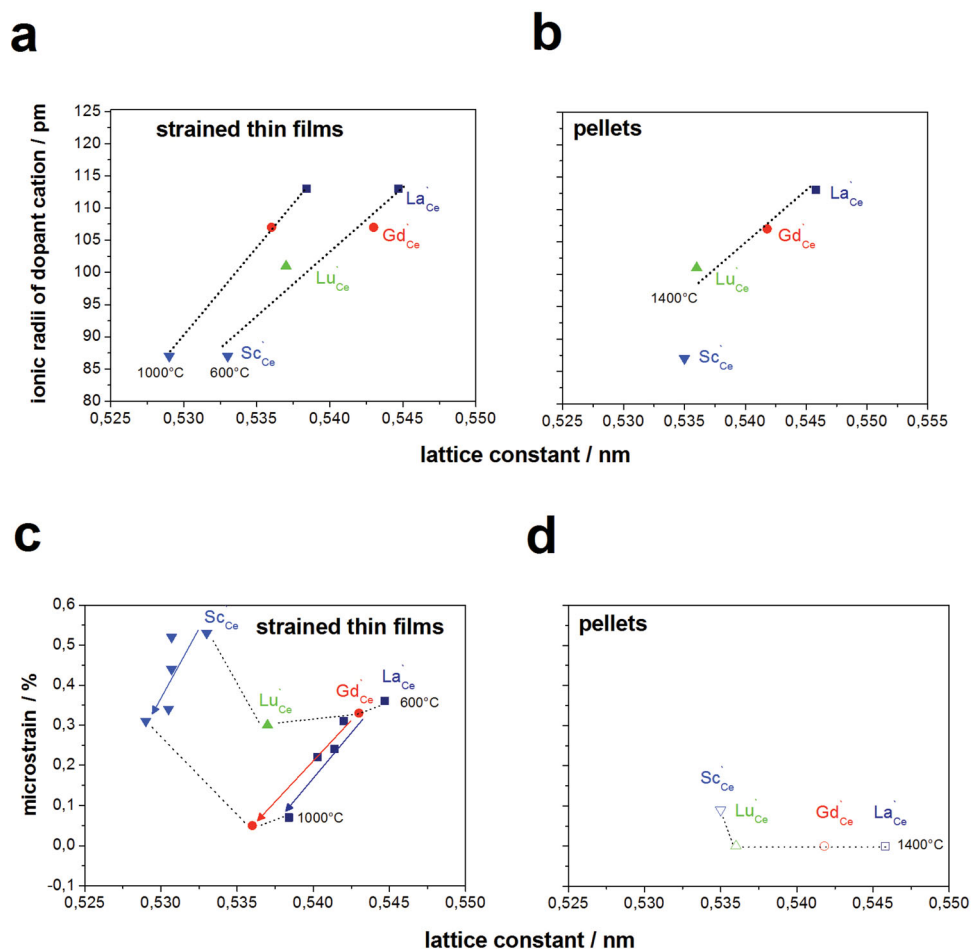


Figure 2. Ionic radii of dopant cation (a,b) and microstrain (c,d) with respect to lattice constant of 20 mol% doped ceria thin films for strained thin films and pellets. Strained thin films are displayed in (a,c) and sintered pellets in (b,d). The thermodynamic equilibration temperatures of the crystal structures are indicated relative to lattice constant for films and pellets by dashed lines.

lower than those of the pellets, i.e. these films are denser, with the degree of compaction dependent on the dopant cation's radius; 2) the changes in lattice constant of thin films induced by post-annealing are on the order of the changes in lattice constant introduced by doping in bulk ceria with substantial changes in dopant ion diameter. Detailed XRD spectra are discussed in Supporting Information I, and these clearly reveal changes in diffraction peak position while heating. The lattice constant change, $\Delta d_{600-1100\text{ }^\circ\text{C}}$, represents the relative change in lattice constant for the annealing temperature range of 600–1100 °C. Overall, it is largest for the smallest dopant cation; viz., $\Delta d_{600-1100\text{ }^\circ\text{C}}$: -1.7% (Sc^{+3}) > -1.5% (Gd^{+3}) > -1.2% (La^{+3}). Upon cooling to room temperature, the last equilibrated lattice constant, induced at the post-annealing temperature, is maintained as a “frozen in” state (outside of thermal expansion contributions). This is in contrast to sintered pellets, where the lattice constant is processing independent. Kossoy et al. reported a similar irreversible lattice constant reduction of $\Delta d_{20-500\text{ }^\circ\text{C}}$: -1.8% for undoped CeO_2 thin films.^[45]

Figure 2a,b compares the lattice constant of the high temperature sintered pellets to the lattice constant change for thin films with the same dopants, but with the widely different

post-anneal conditions of between 600 and 1000 °C. The lattice constant of the $\text{M}_{0.2}\text{Ce}_{0.8}\text{O}_{1.9-x}$ pellets increases from 0.535 to 0.545 nm, when going from Sc to La (Figure 2b). This corresponds to a lattice constant change of $\Delta d = 0.01$ nm, arising from the change of dopant cationic radii size by $\Delta r = 17$ pm. Lanthanide-doped thin films reveal, for the same processing history (e.g., 600 °C anneal), a comparable slope of the straight line fit for dopant radii relative to lattice constant (Figure 2a). Generally, one expects a linear fit of lattice constant versus dopant ionic radii for a fixed concentration of dopant. This holds largely true for the tested lanthanide dopants in the ceria pellets as shown in Figure 2b. For scandia doping, an anomalous deviation from this linear dependence is found, as this material exhibits an increased lattice constant relative to the linear extrapolation derived from the other compositions. This may be related to the formation of $(\text{ScV}_\text{O})^\cdot$ clusters, driven by the smaller ionic radius of Sc.^[85,86] Importantly, inspection of the relative lattice constant change in the films, for a given dopant cation radius, for example $\text{Gd}_{0.2}\text{Ce}_{0.8}\text{O}_{1.9-x}$ (see Figure 2a), shows a large drop in lattice constant from 0.536 to 0.543, following post-annealing treatments between 1000 °C and 600 °C. This corresponds to a relative lattice constant change of

$\Delta d = \Delta 0.007$ nm. Thus, up to 2/3 of the lattice constant change observed for a pellet, when covering the large radius range from Sc to La, can be reproduced by varying the post-annealing temperatures alone in a thin film of fixed composition.

Through the XRD patterns and also SEM images (Supporting Information) an average grain size of approximately 10 and 20 nm was found for anneals performed at 600 and 1000 °C, respectively, independent of dopant kind (for 20 mol% Sc, Lu, Gd, and La in ceria). We note that the grain size increased by a factor of two during the above mentioned anneals.

In the following, the microstrain, bond length (representative of bond strength) and ionic conductivity characteristics of $M_{0.2}Ce_{0.8}O_{1.9-x}$ ($M = Sc^{3+}, Lu^{3+}, Gd^{3+}$ or La^{3+}) solid solutions are presented as a function of lattice constant, both for thin films with different post-anneal temperatures, and for bulk pellets previously sintered at elevated temperatures. (Since a small deviation from stoichiometry is expected, experiments are carried out in air and for high extrinsic dopant concentrations, chemical formula for films and pellets is denoted by general form of $M_{0.2}Ce_{0.8}O_{1.9-x}$.)

Microstrain is next investigated to evaluate the role of doping and post-anneal temperature treatments on lattice distortions (for pellets vs films), Figure 2c,d. Microstrain describes the isotropic displacement fields of atoms in a material, affecting local variations in ionic bond lengths.^[87–89] Williamson-Hall methods are used to extract values for microstrain from the analysis of peak width broadening in X-ray diffraction patterns.^[90,91] In the context of oxygen diffusion, the presence of a non-zero microstrain in the material implies that the local atomic environment around an oxygen vacancy is varied, and thus, a range of migration energy barriers can be expected, rather than a single value. All lanthanide pellets investigated reveal 0% microstrain, within the error of measurement, except for scandia doping, see Figure 2d (open symbols), in agreement with the published literature.^[92–96] This follows from the high sintering temperatures attained, for which equilibrium lattice positions are established for the cations, leading to zero microstrain. For comparison, microstrain for thin films is shown with respect to post-anneal temperature in Figure 2c. Here, the microstrain differs from zero. Indeed, we observe that microstrain is highest for the lowest post-anneal temperature, and that microstrain decreases as the post-anneal temperature is increased. Even though the films appear fully crystalline (Supporting Information), they retain microstrains of up to 0.3–0.55%, that relax upon annealing from 600 to 1000 °C. Microstrains can be relaxed to nearly 0% by post-annealing at 1000 °C, except for the case of scandia doping. In the latter case, the film lattice is under contraction and the highest microstrain levels are measured among this series of dopants. The effective microstrain state depends not only on the post-anneal history, but, also, on the film dopant–host cation radius mismatch. A minimum in microstrain exists for a low radius mismatch, as is the case for $Lu_{C_{Ce}}$ doping. Microstrain increases with increasing dopant–host radius mismatch, as for $La_{C_{Ce}}$ or $Sc_{C_{Ce}}$.

The lattice constant and microstrain capture changes mainly in the cation sublattice for a given single phase.^[92] Recent computational work has drawn attention to the importance of cation-anion bond strength in the oxide-ion diffusion process.^[60] For migration to proceed, the local cation-oxygen bonds must

be broken; the weaker the local bonds, the easier to migrate with a lower migration energy barrier. Here we use Raman spectroscopy, a powerful tool for probing the relative changes in cation-anion distances, or bond lengths, with respect to strain and size of the dopant cation. For a given crystal structure and composition, the increase (decrease) of bond lengths are associated with the weakening (strengthening) of those bonds. The thin film fluorite oxides studied here have only a single allowed triply degenerated F_{2g} Raman mode, viewed as a symmetric breathing mode of the oxygen ions around each cation^[97] (see Figure 1a for the indicated Raman bond). Because the cation-anion bond strength is inversely proportional to bond length, probed via the Raman shift of the F_{2g} mode, the data is complementary to the information derived from the cubic lattice constant, as measured in XRD. Undoped CeO_{2-x} pellets are well characterized in the Raman spectroscopy literature by the processing insensitive F_{2g} mode of 465 ± 1 cm^{-1} .^[98] Doping with larger acceptor cations leads to the shift of this mode towards lower wavenumbers, resulting from lattice expansion,^[99] as demonstrated for the dopants La, Nd, Eu, Gd, Tb, Pr, Ho, or Sm in ceria.^[98,100–103] While the Raman “footprint” characteristics are well investigated for bulk ceramics, the same does not apply to thin films. In Figure 3, the Raman characteristics of doped ceria are compared in pellets vs. strained films. $Ce_{0.8}Sc_{0.2}O_{1.9-x}$ Raman spectra are displayed for the pellet and the thin films with two different lattice constants. The largest Raman F_{2g} wavenumber of 465 cm^{-1} (Figure 3d) was measured for the pellet ($d = 0.535$ nm). Compared to the pellets, the F_{2g} wavenumber decreases in thin films (Figure 3c), to 447 and 452 cm^{-1} for the lattice constants of 0.533 and 0.525 nm (annealed at 600 and 1000 °C), respectively.

Among these films, we observe that as the lattice constant decreases, the wavenumber of F_{2g} increases. This is consistent with a lattice compaction and strengthening of local cation-anion bonds. Interestingly, the shifts in the peak position measured for the films, with respect to the pellet, are larger ($\Delta F_{2g} = 8$ cm^{-1}). To illustrate this point, we plot all Raman F_{2g} shifts for pellets (Figure 3d) and films (Figure 3c) as a function of the four different dopants tested (Sc, Lu, Gd, and La) Figure 3c,d. The relative Raman spectra are detailed in Supporting Information IX. First, in pellets, for small dopant–host radius mismatch, that is, $Lu_{C_{Ce}}$ substitution, the F_{2g} mode frequency is nearly equal to that measured for undoped $Ce_{C_{Ce}}$ at 465 cm^{-1} .^[104] However, when larger dopant cations are used, such as $La_{C_{Ce}}$, the resulting lattice expansion shifts the F_{2g} mode to 456 cm^{-1} . A comparison with the data from the literature on doped ceria pellets reveals a good agreement with the present measurements on $La_{C_{Ce}}$,^[98,100] $Lu_{C_{Ce}}$,^[99] and $Gd_{C_{Ce}}$,^[105–107] within an error of ± 1 cm^{-1} . This demonstrates that lattice expansion (+1.83%) caused by La doping (radius misfit of +16%) leads to a stretching and weakening of the oxygen-cation bond by $\Delta F_{2g} = 9 \pm 1$ cm^{-1} (+1.94%) relative to the undoped case. The study of doped ceria thin films reveals that up to $\Delta F_{2g} = 4 \pm 1$ cm^{-1} Raman shifts are found for a given dopant when the lattice parameter is varied by post-annealing, Figure 3c,d. This is a remarkable relative change that would correspond to doping with, for example, a dopant 8% larger in radius than the host cation! We observe, for a given doped thin film, that, in parallel to reduction of lattice constant, the Raman F_{2g} peak shifts to

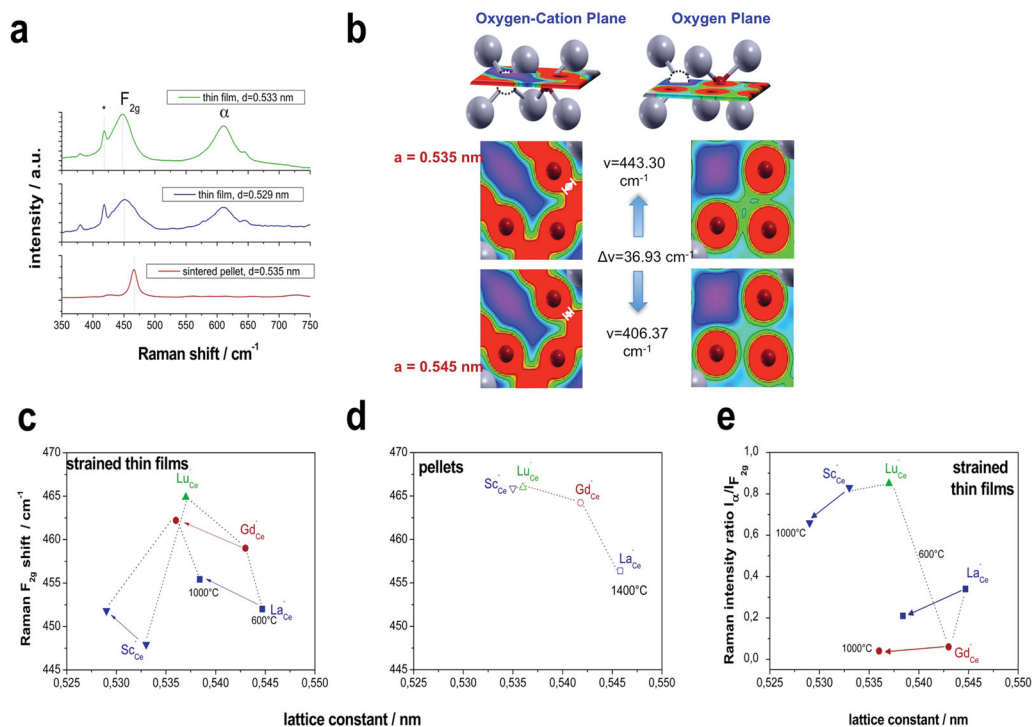


Figure 3. Raman near order characteristics of 20 mol% doped ceria thin films and pellets with respect to lattice constant. a) Exemplary Raman spectra for $\text{Ce}_{0.8}\text{Sc}_{0.2}\text{O}_{1.9-x}$ pellet versus thin films at two different frozen-in microstructures (annealed at 600 and 1000 °C prior to Raman). b) Computation of the Raman shift as a function of lattice strain for ceria. Visualized planes corresponds to the F_{2g} Raman mode probed relative to lattice constant for anion-cation bonds, and oxygen planes. c,d) Experimentally determined F_{2g} Raman shifts of strained ceria solid solution films and sintered pellets with respect to lattice constant. e) Raman phonon scattering on oxygen vacancies in strained ceria films with respect to lattice constant (intensity ratio relative to F_{2g} Raman mode intensity). The thermodynamic equilibration temperatures of the crystal structures are indicated relative to lattice constant for films and pellets by dashed lines.

higher wave numbers, indicating lattice contraction and anion-cation bond strengthening. Thus we deduce that the oxygen-cation bond strength can apparently be engineered through both post-annealing and doping in these films, and both tuning parameters have comparably significant effects. In Figure 3b, our DFT calculations also show that the lattice expansion due to hydrostatic strain weakens the anion-cation bond strength, represented by the width of the charge density distribution between O and Ce.

Based on this observation, the next question addressed is how the changed anion-cation bond distance and lattice parameters impact oxygen vacancy concentration and migration. It is known in the literature that a second Raman band, attributed to second order phonon scattering on oxygen vacancies, increases with increasing concentration of dopants in ceria.^[98] The intensity of this band was correlated to the oxygen vacancy concentration in ceria induced by extrinsic doping. This band is also found around 530–600 cm^{-1} in the samples examined here (assigned as α), Figure 3a. Thin films show an increase in the intensity of this peak, for large lattice constants (low packing density, high strains) for each dopant, Figure 3e. Recently, Pikalova et al.^[99] described, for the first time, that a slight red shift in the α -peak position and changes in the α -peak intensity are observed when varying the dopant cation radius. The authors hypothesized that “changes in intensities are related to the size of the vacancies, which increases with effective radii of the dopant” for comparable lanthanoide pellets at a constant

dopant concentration^[99] changes in intensities and mode shifts may be attributed to the different oxygen migration space as a function of dopant radii.

The dependence of the ionic conductivity of acceptor doped ceria solid solutions on dopant type and post-anneal history (for thin films) is discussed in the following. Microfabricated interdigitated thin film electrode geometries and painted electrodes were used to monitor the electrical conductivity of the strained thin film and sintered pellets, respectively (Figure 4a). The Arrhenius dependence of the total bulk electrical conductivity of the $\text{Ce}_{0.8}\text{M}_{0.2}\text{O}_{1.9-x}$ ($\text{M} = \text{Sc}^{3+}, \text{Lu}^{3+}, \text{Gd}^{3+}, \text{La}^{3+}$) pellets on reciprocal temperature examined in this study is plotted in Figure 4b. The analyses of the complex impedance spectra and the separation of grain boundary and bulk contributions for pellets are detailed in Supporting Information.

Previous studies confirm that for these high dopant concentrations (20 mol%), the conductivity measured in air is predominantly ionic, resulting from oxygen ion migration via vacancy sites ($\text{V}_{\text{O}}^{\cdot\cdot}$). A clear maximum in total conductivity and minimum in activation energy of 0.74 eV is observed, in Figure 4b, for gadolinium doping. The activation energy increases both for larger dopant cations, for example, 0.96 eV for lanthanum, and smaller dopants, for example, 1.13 and 1.53 eV for lutetium and scandium doping respectively. This is in agreement with the findings reported in the literature for bulk ceria^[11,13,108,109] with the trend explained in terms of cation-vacancy association effects. The available literature on pellets usually discusses bulk

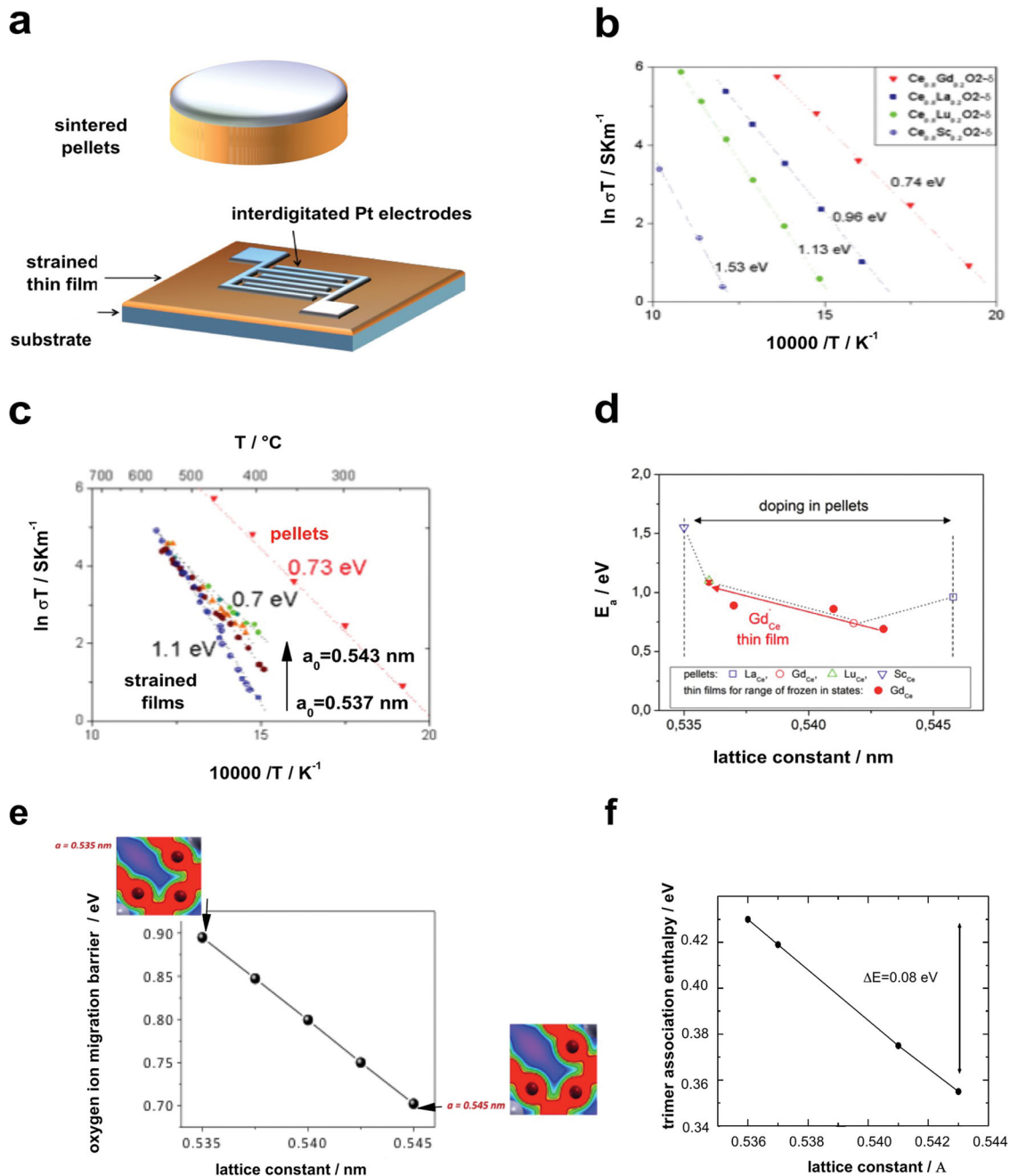


Figure 4. Electrical conductivity of 20 mol% doped ceria thin films and pellets. a) Measurement set-up pellet vs thin film samples with microabricated sputtered electrodes. b) Arrhenius diagrams for electrical conductivity of $\text{Ce}_{0.8}\text{M}_{0.2}\text{O}_{1.9-x}$ pellets with $\text{M} = \text{Sc}, \text{Lu}, \text{Gd},$ or La . c) Arrhenius diagram of $\text{Ce}_{0.8}\text{Gd}_{0.2}\text{O}_{1.9-x}$ thin films on sapphire and MgO substrates for different frozen in states (lattice constant). d) Activation energy of total conductivity in air range for $\text{Ce}_{0.8}\text{M}_{0.2}\text{O}_{1.9-x}$ pellets doped with $\text{M} = \text{Sc}, \text{Lu}, \text{Gd},$ or La plotted relative to the ones of $\text{Ce}_{0.8}\text{Gd}_{0.2}\text{O}_{1.9-x}$ thin films in different frozen in states. (e) Computed DFT oxygen ion migration barrier relative to lattice constant for undoped ceria. f) Computed DFT trimer dopant-vacancy enthalpy relative to lattice constant for $\text{Ce}_{0.8}\text{Gd}_{0.2}\text{O}_{1.9-x}$. The range of frozen in structural states is indicated by an arrow pointing from minimum (600 °C) to maximum (1000 °C) post-anneal temperature probed for thin films.

ionic transport in terms of lattice constant.^[11] Changes in lattice constant through dopant-host radii mismatch reportedly impact defect association for a given solute concentration as reviewed in the Introduction. In the following, we compare our experimental findings on the ionic conductivity versus lattice

constant, for a range of dopants in bulk pellets, and for gadolinia-doped ceria thin films with various processing-dependent lattice constants.

A comparison of the dependence of the ionic conductivity versus reciprocal temperature of the $\text{Ce}_{0.8}\text{Gd}_{0.2}\text{O}_{1.9-x}$ pellets and

thin films measured in air is presented in Figure 4c. The thin film data is further presented by the dependence of activation energy on lattice constant, obtained from the various annealing treatments (Figure 4d). At temperatures below 500 °C, the ionic conductivity activation energy in GDO films increases from 0.7 to 1.1 eV, with a reduction in lattice constant from 0.543 to 0.536 nm. In accordance with the observed increase in the activation energy, a lowered conductivity is measured. At temperatures above 500 °C, the conductivities of all the films, annealed at the various temperatures, appear to converge. While it appears that all the curves converge to a single activation energy of 0.7 ± 0.1 eV, independent of their frozen-in lattice constant, there is insufficient data at elevated temperatures to distinguish this possibility from one in which the curves happen to cross each other in the 500–600 °C range and would result in different pre-exponential factors according to the Meyer-Neldel rule.^[110] For thin films, it remains difficult to isolate grain boundary from grain contributions in the EIS data. However, the fact that grain size increased upon annealing (from 10 to 20 nm), normally leading to a reduced resistance due the decreased number of series grain boundaries, while the overall resistance of these films increased upon lattice compaction with annealing, provides strong evidence that grain boundaries contribute, at most, in a minor way to the observed trends in conductivity.

The reproducibility of these results were confirmed by remeasuring the electrical conductivity on the same sample (for film with largest lattice constant) with activation energy within an error of ± 0.03 eV. To eliminate the possibility of the substrate effects (i.e., chemical interdiffusion or substrate-film strain), a new set of $\text{Ce}_{0.8}\text{Gd}_{0.2}\text{O}_{1.9-x}$ thin films were deposited on a different substrate material (MgO single crystal), post-annealed at 1000 °C, followed by deposition of new interdigitated electrodes. An excellent match of the ionic conductivity activation energy, within an error of ± 0.02 eV, was found for the 550 nm thick films on MgO and those deposited onto sapphire single crystal substrates. The changes in the activation energy of the $\text{Ce}_{0.8}\text{Gd}_{0.2}\text{O}_{1.9-x}$ thin film with change in its lattice constant can thus be attributed to the metastable nature of these polycrystalline microstructures, and not resulting from chemical interdiffusion, differing growth conditions or strain induced at the substrate-film interface. It is also to be noted that the thin films exhibit a conductivity that is at least one order of magnitude lower than that of the pellets. Similar observations have previously been made in the solid state ionics literature where polycrystalline films reveal generally lowered ionic conduction than the bulk material^[47,51,78,111,112] for zirconia and ceria, though several reports, stating the contrary, can also be found.^[12,52] Sanna et al. reported on increased conductivity for epitaxial films, and a lowered one for polycrystalline thin film microstructures.^[113]

The change in the activation energy as a function of the lattice constant for $\text{Ce}_{0.8}\text{Gd}_{0.2}\text{O}_{1.9-x}$ thin films is reported in Figure 4d for $T < 500$ °C. These data are compared with changes in the activation energy observed when doping with different cations in $\text{Ce}_{0.8}\text{M}_{0.2}\text{O}_{1.9-x}$ ($M = \text{Sc}^{3+}, \text{Lu}^{3+}, \text{Gd}^{3+}, \text{La}^{3+}$) bulk pellets. The impact of the lattice constant of $\text{Ce}_{0.8}\text{Gd}_{0.2}\text{O}_{1.9-x}$ thin films on the activation energy was found to coincide well (within ± 0.03 eV) with the relative changes observed in the pellets upon change in dopant cation radius.

We iterate that this is a significant effect induced solely by post-processing of the thin films.

3. Discussion

Despite the growing interest in the ionic conduction properties of doped ceria thin films, unequivocal elucidation of structural near and long range order changes, and implication for the ionic diffusivities, have not been achieved, particularly with respect to processing-dependent lattice constants. Thin film crystal structures have not reached equilibrium due to the low processing and post-annealing temperatures and compact upon annealing. It is not possible to ascribe, for example, equal ionic diffusion kinetics for a material processed in the form of a thin film or a pellet, if their lattice parameter and oxygenation bond strength (Raman characteristics) differ strongly, as demonstrated here in Figure 1b, 3c. Two independent measurements, XRD and Raman spectroscopy (Figure 1b, 3c respectively), reveal that thin film lattices compact upon increase in post-anneal temperature. This holds for all investigated doping cations in this study, namely scandium, lutetium, lanthanum and gadolinium, and maybe related to defect clustering effects.^[114–116] Simultaneously, microstrain also decreases in all thin film crystal structures with increasing post-anneal temperature Figure 2c. This compaction of the lattice decreases the space available for oxygen migration, and as demonstrated computationally relative to shifts in the Raman F_{2g} vibrational modes, increases the local cation-oxygen bond strengths, thereby raising the oxygen ion migration barrier, Figure 3b. This finding resulted from computation of the Raman shifts (near order bonds) relative to the lattice compaction in the films and supports the experimental findings. Concerning the ionic conductivity, an increase in the activation energy from 0.7 to 1.1 eV was measured for gadolinia-doped thin films with decreasing lattice parameter from 0.543 to 0.536 nm, Figure 4d.

In an attempt to rationalize these results, namely the fact that the same material presents different activation energies (0.7–1.1 eV) at low temperature, depending on the post-anneal temperature, we take a closer look at the activation energy of these materials and the factors affecting it. We recall that the activation energy for the oxide-ion conduction contains two contributions, migration barrier and defect association energies (see Equation 2). The defect association energy ΔH_a , in turn, can be further divided into two contributions, one coming from the interaction between a vacancy and the dopant cation ($\Delta H_{\text{cat-rac}}$) and another one from the interaction between a vacancy and neighboring vacancies ($\Delta H_{\text{vac-vac}}$).^[84,117–119] In the following, we apply DFT calculations, and an analysis of the literature, to examine the relative changes of the migration and association enthalpies as a function of lattice parameter (representing a hydrostatic lattice strain) in gadolinia-doped ceria. Strain is known to affect the migration enthalpy of oxygen ions in the fluorite and perovskite lattices, as reported in a number of recent studies.^[40,59,60,79,120–123] Our DFT calculations on pure CeO_2 , shown in Figure 3b, clearly indicate that a $\approx 2\%$ strain (within the same range of the experimentally determined lattice parameters in this work) yields a change in the migration energy barrier of approximately 0.2 eV, about half of the experimentally

observed change of ≈ 0.4 eV in Figure 4c, but the same order of magnitude. This analysis would be appropriate only if the experimental activation energy were solely determined by the migration energy, thereby assuming that the convergence in the conductivity curves in Figure 4c above ≈ 500 °C was coincidental. Alternatively, convergence to a single activation energy at elevated temperatures implies a constant migration energy with higher activation energies at lower temperatures indicative of defect association/ordering. We focus here on assessing the vacancy-cation association effects, that is, on the $\Delta H_{\text{cat-vac}}$ term. In previous work using Molecular Dynamics simulations in Y-doped CeO₂, we found that isotropic strain has virtually no effect on vacancy-vacancy ordering, $\Delta H_{\text{vac-vac}}$.^[124] Figure 4f shows the association energy for a (Gd-V-Gd) trimer in Gd-doped CeO₂, for different values of the lattice parameter. These values are the same as the experimentally determined lattice parameters for Gd-doped CeO₂ thin films in this work. As the lattice is compressed, the association energy of the trimer is predicted to increase by as much as 0.08 eV. Similar calculations (not shown) for a dimer, that is, (Gd-V), yield an energy of 0.04 eV. This change of nearly 0.1 eV observed for the trimer (0.04 eV calculated for the dimer), is in agreement with a recent study by Rushton et al. who observed a similar change.^[125] While this is in qualitative agreement with the trend observed in these thin films, these values are significantly lower than the 0.4 eV change in the activation energy measured by impedance spectroscopy. One should stress, however, that the studied defect associate (a vacancy-cation dimer and a cation-vacancy-cation trimer) is rather simplistic and that, for the high concentrations of defects, such as in this case (5% oxygen vacancies), more complicated defect clusters are expected.^[114–116] In conclusion, based on computer modeling, the large change in activation energy observed in these films with lattice compression appears to be more consistent with the expected effects of compressive strain on the migration energy of oxygen vacancies, although the corresponding impact on defect association/ordering (especially if extended) cannot be excluded.

4. Conclusions

The growing interest in integrating thin film solid electrolytes and mixed ionic electronic conductors into Si-based microsystems for the development of micro solid oxide fuel cells, micro-batteries, micro sensor arrays or resistive switches draws attention to how the properties of such films, which must be fabricated and/or operated below 500–700 °C, influence their long term performance. It becomes particularly important to understand how these limitations impact the transport properties of these films, particularly those of the oxygen ion and their dependency on the processing dependent lattice compression or expansion. In this systematic investigation of the oxygen ion conductivity of both bulk and thin film acceptor doped ceria as a function of acceptor dopant diameter ($M_{0.2}\text{Ce}_{0.8}\text{O}_{1.9-x}$ ($M = \text{Sc}^{3+}, \text{Lu}^{3+}, \text{Gd}^{3+}$ or La^{3+})), we discovered a major dependence of lattice parameter of the thin films, not only on acceptor diameter, as expected, but also on the post growth anneal temperature. Following a 600 °C anneal of the films deposited at room temperature, they exhibit lattice parameters close to those

of their bulk counterparts. With increasing anneal temperature, however, the films exhibited substantial compaction with lattice parameters decreasing by as much as nearly 2% (viz, $\Delta d_{600-1100\text{ °C}}$: -1.7% (Sc^{3+}) $>$ -1.5% (Gd^{3+}) $>$ -1.2% (La^{3+})) for the annealing temperature range of 600–1100 °C. Remarkably, 2/3 of the lattice parameter change obtained in sintered bulk ceria upon changing the acceptor diameter from the smaller Sc to larger La, can be reproduced by post annealing a film with fixed dopant diameter and composition. We therefore investigated the ionic conductivity of gadolinia-doped ceria thin films and found that the activation energy of ionic conductivity increases as the lattice parameter of the film decreases. In an attempt to rationalize this experimental finding, two possible mechanisms have been tested by DFT calculations; the increased migration barrier and the increased defect association energy to form dimers or trimers. While the impact of lattice compaction on defect association/ordering cannot be entirely excluded, the main effect appears to result in an increase in migration energy and consequent drop in ionic conductivity.

A review of the literature demonstrates that there is a large discrepancy in the reported electrical and mechanical characteristics of both supported and free-standing thin film membranes; see.^[126,127] Based on the results reported in this study, it is highly likely that these discrepancies result from differing frozen in metastable states of the thin films. More generally, these results point to the importance of understanding the electro-chemo-mechanical coupling that goes on in such materials, that is, the tie in between mechanical strain, chemical stoichiometry and electrical charge carrier concentration and transport.^[80] At least from the standpoint of acceptor doped ceria films, it is clear that annealing procedures should be held to a minimum to maintain the optimum oxygen ion conductivity and specifically the low migration energy of the oxygen ions for energy-related applications.

5. Experimental Section

5.1. Material Synthesis

$M_{0.2}\text{Ce}_{0.8}\text{O}_{1.9-\delta}$ ($M = \text{Sc}, \text{Lu}, \text{Gd}$ or La) powders, pellets, and thin films were synthesized in this study.

Powder Processing: The nanocrystalline powders were synthesized by a modified sol–gel process. Stoichiometric amounts of commercial $\text{Ce}(\text{NO}_3)_3 \cdot 6\text{H}_2\text{O}$ (Aldrich, 99.99%) and Sc_2O_3 (Aldrich, 99.9%), or Lu_2O_3 (Aldrich, 99.9%), or $\text{Gd}(\text{NO}_3)_3 \cdot 6\text{H}_2\text{O}$ (Aldrich, 99.9%), or $\text{La}(\text{NO}_3)_3 \cdot 6\text{H}_2\text{O}$ (Aldrich, 99.99%) were dissolved in an aqueous solution of nitric acid. Citric acid was used as a chelating agent in a 2:1 ratio with respect to the total metal cations. After obtaining a transparent solution, the pH was adjusted between 6 and 8 by adding NH_4OH . The solution was heated under stirring and finally ignited to flame, resulting in a grey ash. The ash was heated to 650 °C for 6 h to form single phase doped-ceria powders.

Pellet Processing: Pechini-derived powders synthesized in this study were used to prepare both bulk pellets and PLD targets. The pellets were produced by uniaxial and isostatically pressing (850 kN for 2 min), and subsequent heating to 1500 °C at 3 °C min⁻¹, maintaining 1500 °C for 4 h and then cooling at 5 °C min⁻¹ to room temperature. The density of the pellets was evaluated using the Archimedes method.

Thin Film Processing: The ceria-based films were deposited on a (001) sapphire single crystal (Stettler company, Switzerland) by pulsed laser

deposition (PLD) using a KrF excimer laser operating at a wavelength of 248 nm. Deposition was established at 350 mJ per pulse at a repetition rate of 10 Hz for a substrate to target distance of 6.5 cm. After reaching a background pressure of 10^{-5} mbar, the films were deposited at room temperature and 10 mbar O_2 pressure. The film thickness was determined by the number of PLD pulses and subsequent profilometer measurements. 90 000 pulses resulted in an average film thickness of 700 nm.

5.2. Electrode Preparation and Microfabrication

Two types of electrodes were used in this study, typified by large-scale electrodes for measurements of sintered pellets, and small-scale micropatterned interdigitated electrodes suitable for high resolution impedance measurements of metal oxide thin films.

Large-Scale Pellet Electrode Preparation for Sintered Pellets: For conductivity measurements, two symmetrical porous Pt electrodes were brush painted onto both sides of polished doped ceria pellets and heated to 1000 °C for 1 h.

Small-Scale Micropatterned Interdigitated Electrodes for Thin Films: Platinum interdigitated electrodes were fabricated by metal lift-off photolithography. After rinsing with acetone and alcohol and drying with N_2 , a photoresist (FUTURREX, inc, NR7-3000, Franklin, NJ) was spin-coated onto the sample surface at a rotation speed of 3000 RPM and baked at 150 °C for two minutes. The samples were then exposed to broadband ultraviolet light for 30 s through a chrome photolithography mask that had a number of different interdigitated electrode designs. After post-baking at 100 °C for two minutes, the samples were soaked in a resist developer (FUTURREX, inc, RD6, Franklin, NJ) until the electrode patterns were completely developed, as determined by visual inspection. Dense platinum films were then RF sputtered onto the photoresist patterns in a Kurt J. Lesker magnetron sputtering system. The sputtering atmosphere was argon, maintained at 5.0 mTorr with a flow rate of roughly 15 sccm at room temperature. 50 W of DC power were used. To dissolve the photoresist and complete the lift-off patterning, the samples were soaked in acetone in a covered dish for a few hours. The smallest electrode distance fabricated in the interdigitated pattern was 12 micrometers.

5.3. Chemical and Structural Characterization

An inductively coupled plasma optical emission spectrometry, ICP-OES (Nippon Jarrel-Ash Co., IRIS Advantage) was used for chemical analysis. Further, the materials were characterized by scanning electron microscopy (SEM, Leo Gemini 1530) to investigate microstructures. In-situ X-ray diffraction (XRD) was carried out on pellets and films using a PANalytical X'Pert Pro multi purpose diffractometer with a heating chamber and a $Cu K_{\alpha}$ wavelength. Heating was carried out at a rate of 3 K min^{-1} , or, for isothermal holds, at constant temperature. The in-situ heating diffractometer was equipped with programmable divergence slits and high resolution X'Celerator position sensitive detector. The microstrain was determined using the Williamson-Hall method after correction for instrumental peak broadening in the total full width of half maximum determined.^[90] In order to determine the instrumentally broadened full width at half maximum contributions as a function of the diffraction angle 2θ , 13 hkl reflections of a LaB_6 (NIST SRM660) standard powder sample were measured as well as microcrystalline non-strained ceria-powders. In-case of powders, ex-situ XRD powder diffractograms were measured using a Rigaku (Ultima III) diffractometer with $Cu K_{\alpha}$ radiation. Raman spectra were recorded with a spectrometer (Kaiser Optical Hololab 5000R Raman Microscope); a solid state laser 400 mW (Invictus) with an excitation wavelength of 785 nm was used in micromode.

5.4. Electrical Characterization

Electrochemical impedance spectroscopy measurements of the sintered pellets were performed in air using a multichannel potentiostat (VMP3,

Bio-Logic Co.), in the 0.1 Hz–1 MHz frequency range, with an applied ac voltage amplitude of 50 mV. For this conventional Pt-paste contacts were applied. The small-scale thin film patterned electrodes were contacted with microprobe tips in a custom fabricated microprobe station with a sealed atmosphere environment, equipped with stereomicroscopy. Impedance spectroscopy measurements were carried out with the aid of a Novocontrol model Alpha-A Impedance analyzer (Hundsangen, Germany) operating with 300 mV amplitude over the frequency range of 10 mHz–1MHz. To distinguish electrode from film response, measurements were carried out with varying bias from zero to 1 V. Equivalent circuits were fitted to the impedance spectra with the aid of Scribner Associates Inc. ZView 2 software (Southern Pines, NC) in a complex mode with calc-modulus weighting. To assure reproducibility of the measurements, the thin films were re-contacted more than 5 times with impedances recorded for more than 3 heating and cooling cycles, at a rather small T increase/cool intervals of 5–10 °C at a heating rate of 5 K/min.

5.5. Computation

Plane wave DFT calculations were performed using the Vienna ab initio simulation package (VASP)^[128] to assess the strain response of the oxygen ion migration barrier, defect association energies and vibrational frequencies of the O–Ce–O bond. We employed the generalized gradient approximation (GGA) parameterized by Perdew-Burke-Ernzerhof (PBE)^[129] along with the projector augmented wave (PAW) method^[130] to describe the ionic cores. A Hubbard term with $U = 5$ eV^[131] was added to Ce to correct for the self-interaction errors present in conventional DFT. Similarly, $U = 5$ eV was also used for Gd, to make sure that the f -electrons of this ion were properly localized. This was subsequently confirmed by checking the spin state and charges of these ions. Our treatment differs slightly from other approaches where a certain number of f -electrons are frozen in the core state to ensure the correct valance,^[21] though we do not anticipate any significant difference. All calculations used a plane wave expansion cutoff of at least 400 eV and included spin polarization. We used a size of $2 \times 2 \times 2$ supercell ($Ce_{32}O_{64}$) derived from the ideal fluorite crystal structure with a $2 \times 2 \times 2$ Monkhorst-Pack k -point mesh. DFT+U has been used extensively for the study of ceria both by authors of this paper and by others,^[119] and has been shown to reproduce very well a range of properties of this material, including lattice parameters, elastic constants, activation energy for ionic conduction and electronic structure.

For the calculation of the migration energy reported in Figure 4, an oxygen vacancy was included in our unit cell. Hydrostatic lattice strain was imposed by changing the lattice constant from 0.535 to 0.545 nm. The climbing image nudged elastic band (CI-NEB) method^[132] was employed to calculate the migration energy barrier of oxygen. Initial approximations to reaction paths were obtained by linear interpolation between the energy minima configurations. Three intermediate images were used, which was sufficient to map the minimum energy path accurately, as also found by other researchers.^[21] Normal modes and vibrational frequencies were calculated within the harmonic approximation using finite difference displacements of 0.005 Å. Among them, the Raman F_{2g} mode was manually assigned by the symmetry of the vibration. 4 Ce–O atoms tetrahedrally connected were included in these calculations but the other atoms were fixed for the computational efficiency. The association energies for a dimer (trimer) was calculated as the difference between a configuration in which the vacancy was nearest-neighbor to the Gd cation(s) and another one in which the vacancy was placed as far as possible (>7 Å) from them.

Supporting Information

Supporting Information is available from the Wiley Online Library or from the author.

Acknowledgements

J.L.M.R. was supported by the Swiss National Research Foundation through the fellowship PP00P2–138914/1. D.M. wishes to thank the Government of Ireland for an EMPOWER Postdoctoral Fellowship and the Trinity Centre for High Performance Computing for computing time. B.Y., H.L.T. and J.W.H. acknowledge the US-DOE – Basic Energy Sciences, Grant No. DE-SC0002633 for financial support, and the National Science Foundation for computational support through the XSEDE Program, Grant No. TG-ASC090058 and TG-DMR110004. J.L.M.R. and H.L.T. acknowledge I2CNER, the WPI initiative, Japan for travel support.

Received: June 21, 2013

Revised: August 30, 2013

Published online: January 3, 2014

- [1] A. Evans, A. Bieberle-Hutter, J. L. M. Rupp, L. J. Gauckler, *J. Power Sources* **2009**, *194*, 119–129.
- [2] R. Tolke, A. Bieberle-Hutter, A. Evans, J. L. M. Rupp, L. J. Gauckler, *J. Eur. Ceram. Soc.* **2012**, *32*, 3229–3238.
- [3] J. Suntivich, H. A. Gasteiger, N. Yabuuchi, H. Nakanishi, J. B. Goodenough, Y. Shao-Horn, *Nat. Chem.* **2011**, *3*, 546–550.
- [4] S. B. Adler, J. A. Lane, B. C. H. Steele, *J. Electrochem. Soc.* **1996**, *3554*.
- [5] M. Kuhn, S. R. Bishop, J. L. M. Rupp, H. L. Tuller, *Acta Mater.* **2013**, *61*, 4277.
- [6] N. Barsan, D. Koziej, U. Weimar, *Sens. Actuators B: Chem.* **2007**, *121*, 18–35.
- [7] R. Waser, M. Aono, *Nat. Mater.* **2007**, *6*, 833–840.
- [8] R. Waser, R. Dittmann, G. Staikov, K. Szot, *Adv. Mater.* **2009**, *21*, 2632.
- [9] U. P. Muecke, D. Beckel, A. Bernard, A. Bieberle-Hütter, S. Graf, A. Infortuna, P. Müller, J. L. M. Rupp, J. Schneider, L. J. Gauckler, *Adv. Funct. Mater.* **2008**, *18*, 3158–3168.
- [10] R. Waser, R. Dittmann, G. Saikov, K. Szot, *Adv. Mater.* **2009**, *21*, 2632–2663.
- [11] M. Mogensen, N. M. Sammes, G. A. Tompsett, *Solid State Ionics* **2000**, *129*, 63–94.
- [12] T. Suzuki, I. Kosacki, H. U. Anderson, P. Colomban, *J. Am. Ceram. Soc.* **2001**, *84*, 2007–2014.
- [13] S. Omar, E. D. Wachsman, J. L. Jones, J. C. Nino, *J. Am. Ceram. Soc.* **2009**, *92*, 2674–2681.
- [14] S. Omar, E. D. Wachsman, J. C. Nino, *Appl. Phys. Lett.* **2007**, *91*, 144106.
- [15] D. Marrocchelli, S. R. Bishop, H. L. Tuller, B. Yildiz, *Adv. Funct. Mater.* **2012**, *22*, 1958–1965.
- [16] M. Burbano, S. T. Norberg, S. Hull, S. G. Eriksson, D. Marrocchelli, P. A. Madden, G. W. Watson, *Chem. of Mater.* **2012**, *24*, 222–229.
- [17] B. Wang, R. J. Lewis, A. N. Cormack, *Acta Mater.* **2011**, *59*, 2035–2045.
- [18] B. Wang, A. N. Cormack, *J. Phys. Chem. C* **2013**, *117*, 146–151.
- [19] D. A. Andersson, S. I. Simak, N. V. Skorodumova, I. A. Abrikosov, B. Johansson, *Proc. Nat. Acad. Sci. U. S. A.* **2006**, *103*, 3518–3521.
- [20] L. Minervini, M. O. Zacate, R. W. Grimes, *Solid State Ionics* **1999**, *116*, 339–349.
- [21] M. Nakayama, M. Martin, *Phys. Chem. Chem. Phys.* **2009**, *11*, 3241–3249.
- [22] R. Röttger, H. Schmalzried, *Solid State Ionics* **2002**, *150*, 131–141.
- [23] Y. Arachi, H. Sakai, O. Yamamoto, Y. Takeda, N. Imanishai, *Solid State Ionics* **1999**, *121*, 133–139.
- [24] A. Kossy, Q. Wang, R. Korobko, V. Grover, Y. Feldman, E. Wachtel, A. K. Tyagi, A. I. Frenkel, I. Lubomirsky, *Phys. Rev. B* **2013**, *87*, 5.
- [25] M. Sugiura, *Catal. Surveys Asia* **2003**, *7*, 77–87.
- [26] J. A. Kilner, *Chem. Lett.* **2008**, *37*, 1012.
- [27] F. Pietrucci, M. Bernasconi, A. Laio, M. Parrinello, *Phys. Rev. B* **2008**, *78*, 094301.
- [28] S. Hull, S. T. Norberga, I. Ahmeda, S. G. Eriksson, D. Marrocchelli, P. A. Madden, *J. Solid State Chem.* **2009**, *182*, 2815–2821.
- [29] T. Mori, J. Drennan, Y. Wang, G. Auchterlonie, J.-G. Li, A. Yago, *Sci. Technol. Adv. Mater.* **2003**, *4*, 213–220.
- [30] T. Mori, J. Drennan, J. H. Lee, J. G. Li, T. Ikegami, *Solid State Ionics* **2002**, *154*, 461–466.
- [31] D. R. Ou, T. Mori, F. Ye, T. Kobayashi, J. Zou, G. Auchterlonie, J. Drennan, *Appl. Phys. Lett.* **2006**, *89*, 171911.
- [32] M. Meyer, N. Nicoloso, *Phys. Chem. Chem. Phys.* **1997**, *101*, 1393–1398.
- [33] M. Meyer, N. Nicoloso, V. Jaenisch, *Phys. Rev. B* **1997**, *56*, 5961–5966.
- [34] A. Murray, G. Murch, C. Catlow, *Solid State Ionics* **1986**, 18–9.
- [35] P. Dholabhai, S. Anwar, J. Adams, P. Crozier, R. Sharma, *J. Solid State Chem.* **2011**, *184*, 811–817.
- [36] D. Beckel, A. Bieberle-Hutter, A. Harvey, A. Infortuna, U. P. Muecke, M. Prestat, J. L. M. Rupp, L. J. Gauckler, Thin Films for Micro Solid Oxide Fuel Cells, *Journal of Power Sources* **2007**, *173*, 325.
- [37] J. Maier, *Phys. Chem. of Ionic Mater.* Wiley **2004**, ISBN 0–470–99991–1.
- [38] I. Lubomirsky, *Monatshefte Fur Chemie* **2009**, *140*, 1025–1030.
- [39] N. I. Karageorgakis, A. Heel, J. L. M. Rupp, M. H. Aguirre, T. Graule, L. J. Gauckler, *Adv. Funct. Mater.* **2011**, *21*, 532–539.
- [40] J. L. M. Rupp, *Solid State Ionics* **2012**, *207*, 1–13.
- [41] B. Scherrer, A. Rossi, J. Martynczuk, M. D. Rossell, A. Bieberle-Hütter, J. L. M. Rupp, R. Erni, L. J. Gauckler, *J. Power Sources* **2011**, *196*, 7372–7382.
- [42] J. L. M. Rupp, U. P. Muecke, P. C. Nalam, L. J. Gauckler, *J. Power Sources* **2010**, *195*, 2669–2676.
- [43] M. J. Madou, Fundamentals of Microfabrication, *The Science of Miniaturization* **2002**: CRC Press Second edition.
- [44] E. D. Wachsman, K. T. Lee, *Science* **2011**, *334*, 935.
- [45] A. Kosoy, Y. Feldman, E. Wachtel, K. Gartsman, I. Lubomirsky, J. Fleig, J. Maier, *Phys. Chem. Chem. Phys.* **2006**, *8*, 1111–1115.
- [46] T. Suzuki, I. Kosacki, H. U. Anderson, *Solid State Ionics* **2002**, *151*, 111–121.
- [47] N. I. Karageorgakis, A. Heel, J. L. M. Rupp, M. H. Aguirre, T. Graule, L. J. Gauckler, *Adv. Funct. Mater.* **2010**, *21*, 532.
- [48] J. L. M. Rupp, B. Scherrer, L. J. Gauckler, *Phys. Chem. Chem. Phys.* **2010**, *12*, 11114–11124.
- [49] B. Scherrer, S. Heiroth, R. Hafner, J. Martynczuk, A. Bieberle-Hütter, J. L. M. Rupp, L. J. Gauckler, *Adv. Funct. Mater.* **2011**, *21*, 3967–3975.
- [50] S. Heiroth, R. Frison, J. L. M. Rupp, T. Lippert, E. J. B. Meier, E. M. Gubler, M. Döbeli, K. Conder, A. Wokaun, L. J. Gauckler, *Solid State Ionics* **2011**, *191*, 12–23.
- [51] I. Kosacki, T. Suzuki, V. Petrovsky, H. U. Anderson, *Solid State Ionics* **2000**, *136*, 1225–1233.
- [52] J. L. M. Rupp, B. Scherrer, A. Harvey, L. J. Gauckler, *Adv. Funct. Mater.* **2009**, *19*, 2790–2799.
- [53] J. L. M. Rupp, B. Scherrer, N. Schauble, L. J. Gauckler, *Adv. Funct. Mater.* **2010**, *20*, 2807–2814.
- [54] I. Kosacki, V. Petrovsky, H. U. Anderson, P. Colomban, *J. Am. Ceram. Soc.* **2002**, *85*, 2646–2650.
- [55] A. Bieberle-Hutter, J. Hertz, H. L. Tuller, *Acta Mater.* **2008**, *56*, 177.
- [56] A. Bieberle-Hutter, P. Reinhard, J. L. M. Rupp, L. J. Gauckler, *J. Power Sources* **2011**, *196*, 6070–6078.
- [57] B. Scherrer, J. Martynczuk, H. Galinski, J. G. Grolig, S. Binder, A. Bieberle-Hütter, J. L. M. Rupp, M. Prestat, L. J. Gauckler, *Adv. Funct. Mater.* **2012**, *22*, 3509–3518.
- [58] J. Garcia-Barriocanal, A. Rivera-Calzada, M. Varela, Z. Sefrioui, E. Iborra, C. Leon, S. J. Pennycook, J. Santamaria, **2008**, *Science* *321*, 676–680.
- [59] N. Schichtel, C. Korte, D. Hesse, J. Janek, *Phys. Chem. Chem. Phys.* **2009**, *11*, 3043–3048.

- [60] A. Kushima, B. Yildiz, *J. Mater. Chem.* **2010**, *20*, 4809–4819.
- [61] Z. W. Wang, D. J. Shu, M. Wang, N. B. Ming, *Phys. Rev. B* **2010**, *82*, 165309.
- [62] R. A. De Souza, A. Ramadan, S. Horner, *Energy Environ. Sci.* **2012**, *5*, 5445–5453.
- [63] D. J. Shu, S. T. Ge, M. Wang, N. B. Ming, *Phys. Rev. Lett.* **2008**, *101*, 116102.
- [64] A. Kushima, S. Yip, B. Yildiz, *Phys. Rev. B* **2010**, *82*, 115435.
- [65] W. Donner, C. Chen, M. Liu, A. J. Jacobson, Y.-L. Lee, M. Gadre, D. Morgan, *Chem. Mater.* **2011**, *23*, 984–988.
- [66] H. Jalili, J. W. Han, Y. Kuru, Z. H. Cai, B. Yildiz, *J. Phys. Chem. Lett.* **2011**, *2*, 801–807.
- [67] Z. H. Cai, Y. Kuru, J. W. Han, Y. Chen, B. Yildiz, *J. Am. Chem. Soc.* **2011**, *133*, 17696–17704.
- [68] J. W. Han, B. Yildiz, *Energy Environ. Sci.* **2012**, *5*, 8598–8607.
- [69] M. Sillassen, P. Eklund, N. Pryds, E. Johnson, U. Helmerson, J. Böttiger, *Adv. Funct. Mater.* **2010**, *20*, 2071–2076.
- [70] H. Aydin, C. Korte, M. Rohnke, J. Janek, *Phys. Chem. Chem. Phys.* **2013**, *15*, 1944–1955.
- [71] D. Pergolesi, E. Fabbri, S. N. Cook, V. Roddatis, E. Traversa, J. A. Kilner, *ACS Nano* **2012**, *6*, 10524–10534.
- [72] T. J. Pennycook, M. J. Beck, K. Varga, M. Varela, S. J. Pennycook, S. T. Pantelides, *Phys. Rev. Lett.* **2010**, *104*.
- [73] G. Dezaneeu, J. Hermet, B. Dupe, *Int. J. Hydrogen Energy* **2012**, *37*, 8081–8086.
- [74] J. A. Hirschfeld, H. Lustfeld, *Phys. Rev. B* **2011**, *84*.
- [75] K. R. Lee, K. Ahn, Y. C. Chung, J. H. Lee, H. I. Yoo, *Solid State Ionics* **2012**, *229*, 45–53.
- [76] S. Sankaranarayanan, S. Ramanathan, *J. Chem. Phys.* **2011**, *134*.
- [77] J. Hinterberg, T. Zacherle, R. A. De Souza, *Phys. Rev. Lett.* **2013**, *110*.
- [78] J. L. M. Rupp, *Solid State Ionics* **2012**, *207*, 1–13.
- [79] J. Santiso, M. Burriel, *J. Solid State Electrochem.* **2011**, *15*, 985.
- [80] H. L. Tuller, S. R. Bishop, *Annu. Rev. Mater. Res.* **2011**, *41*, 369.
- [81] M. L. Lee, A. J. Pitera, E. A. Fitzgerald, *J. Vacuum Sci. Technol.* **2004**, *22*, 158.
- [82] Z. D. Dohcevic-Mitrovic, M. J. Scepanovic, M. U. Grujic-Brojcin, Z. V. Popovic, S. B. Boskovic, B. M. Matovic, M. V. Zinkevich, F. Aldinger, *Solid State Commun.* **2006**, *137*, 387–390.
- [83] R. Korobko, C.-T. Chen, S. Kim, S. R. Cohen, E. Wachtel, N. Yavo, I. Lubomirsky, *Scripta. Mater.* **2012**, *66*, 155–158.
- [84] G. Balducci, M. S. Islam, J. Kaspar, P. Fornasiero, M. Graziani, *Chem. Mater.* **2003**, *15*, 3781–3785.
- [85] R. Gerhardt-Anderson, F. Zamani-Noor, A. S. Nowick, C. R. A. Catlow, A. N. Cormack, *Solid State Ionics* **1983**, *9–10*, 931–936.
- [86] P. Li, I. W. Chen, J. E. Pennerhahn, T. Y. Tien, *J. Am. Ceram. Soc.* **1991**, *74*, 958–967.
- [87] P. Scherrer, *Mathematisch-physikalische Klasse* **1918**, *1*, 98–100.
- [88] A. J. C. Wilson, *Acta Crystallograph.* **1949**, *2*, 318–321.
- [89] E. Zolotoyabko, J. L. M. Rupp, L. J. Gauckler, *Scripta. Mater.* **2012**, *66*, 190.
- [90] W. Hall, G. K. Williamson, *Acta Metall.* **1953**, *1*, 22–31.
- [91] H. Natter, M. Schmelzer, M.-S. Löffler, C. E. Krill, A. Fitch, R. Hempelmann, *J. Phys. Chem. B* **2000**, *104*, 2467–2476.
- [92] W. Kleber, H.-J. Bautsch, J. Bohm, Einführung in die Kristallographie: Chapter 3: Physikalisch-chemische Kristallographie. **1998**, ISBN 3-341-01205-2, 200–204.
- [93] N. Brown, K. F. Lukens, *Acta Metall.* **1961**, *9*, 106.
- [94] S. Forest, R. Sievert, *Int. J. Solids Struct.* **2006**, *43*, 7724.
- [95] J. L. M. Rupp, A. Infortuna, L. J. Gauckler, *Acta Mater.* **2006**, *54*, 1721–1730.
- [96] E. Zolotoyabko, J. P. Quintana, *Beam Interactions with Mater. and Atoms* **2003**, *200*, 382–389.
- [97] W. H. Weber, K. C. Hass, J. R. McBride, *Phys. Rev. B* **1993**, *48*, 178–185.
- [98] J. R. McBride, K. C. Hass, B. D. Poindexter, W. H. Weber, *J. Appl. Phys.* **1994**, *76*, 2435–2441.
- [99] E. Y. Pikalova, A. A. Murashkina, V. I. Maragou, A. K. Demin, V. N. Strekalovsky, P. E. Tsiakaras, *Int. J. Hydrogen Energy* **2011**, *36*, 6175–6183.
- [100] L. Li, F. Chen, J. Q. Lu, M. F. Luo, *J. Phys. Chem. A* **2011**, *115*, 7972–7977.
- [101] G. Gouadec, P. Colombar, *J. Raman Spectrosc.* **2007**, *38*, 598–603.
- [102] G. Gouadec, P. Colombar, *Prog. Crystal Growth Charact. Mater.* **2007**, *53*, 1–56.
- [103] M. Kitajima, *Critical Rev. Solid State Mater. Sci.* **1997**, *22*, 275–349.
- [104] J. E. Spanier, R. D. Robinson, F. Zheng, S. W. Chan, I. P. Herman, *Phys. Rev. B* **2001**, *64*.
- [105] A. Kossov, Y. Feldman, R. Korobko, E. Wachtel, I. Lubomirsky, J. Maier, *Adv. Funct. Mater.* **2009**, *19*, 634–641.
- [106] J. L. M. Rupp, T. Drobek, A. Rossi, L. J. Gauckler, *Chem. Mater.* **2007**, *19*, 1134–1142.
- [107] R. C. Maher, et al. in *Xxii International Conference on Raman Spectroscopy* Vol. 1267 AIP Conference Proceedings, 550.
- [108] H. Yahiro, K. Eguchi, H. Arai, *Solid State Ionics* **1989**, *36*, 71–75.
- [109] J. A. Kilner, *Solid State Ionics* **1983**, *8*, 201–207.
- [110] T. Dosdale, R. J. Brook, *Solid State Ionics* **1983**, *8*, 297.
- [111] S. Heiroth, T. Lippert, A. Wokaun, M. Döbeli, J. L. M. Rupp, B. Scherrer, L. J. Gauckler, *J. Eur. Ceram. Soc.* **2010**, *30*, 489–495.
- [112] A. Infortuna, A. S. Harvey, L. J. Gauckler, *Adv. Funct. Mater.* **2008**, *18*, 127–135.
- [113] S. Sanna, V. Esposito, D. Pergolesi, A. Orsini, A. Tebano, S. Licocchia, G. Balestrino, E. Traversa, *Adv. Funct. Mater.* **2009**, *19*, 1713–1719.
- [114] B. Wang, *Acta Mater.* **2011**, *59*, 2035.
- [115] F. Ye, *Solid State Ionics* **2008**, *179*, 1962.
- [116] F. Ye, *Solid State Ionics* **2009**, *180*, 1127.
- [117] S. Hull, S. T. Norberg, I. Ahmed, S. G. Eriksson, D. Marrocchelli, P. A. Madden, *J. Solid State Chem.* **2009**, *182*, 2815.
- [118] D. Marrocchelli, P. A. Madden, S. T. Norberg, S. Hull, *Chem. Mater.* **2011**, *23*, 1365.
- [119] S. T. Norberg, S. Hull, I. Ahmed, S. G. Eriksson, D. Marrocchelli, P. A. Madden, P. Li, J. T. S. Irvine, *Chem. Mater.* **2011**, *23*, 1356–1364.
- [120] J. W. Han, H. Jalili, Y. Kuru, Z. H. Cai, B. Yildiz, *Solid Oxide Fuel Cells* **2011**, *12*, 2097–2104.
- [121] A. Chronos, B. Yildiz, A. Tarancon, D. Parfitt, J. A. Kilner, *Energy Environ. Sci.* **2011**, *4*, 2774–2789.
- [122] C. Korte, A. Peters, J. Janek, D. Hesse, N. Zakharov, *Phys. Chem. Chem. Phys.* **2008**, *10*, 4623.
- [123] N. Schichtel, C. Korte, D. Hesse, N. Zakharov, B. Butz, D. Gerthsen, J. Janeka, *Phys. Chem. Chem. Phys.* **2010**, *12*, 14596–14602.
- [124] D. Marrocchelli, **2013**, unpublished.
- [125] M. J. D. Rushton, A. Chronos, S. J. Skinner, J. A. Kilner, R. W. Grimes, *Solid State Ionics* **2013**, *230*, 37–42.
- [126] A. Evans, A. Bieberle-Hütter, H. Galinski, J. L. M. Rupp, T. Ryll, B. Scherrer, R. Tölke, L. J. Gauckler, *Chem. Monthly* **2009**, *140*, 975.
- [127] A. Evans, A. Bieberle-Hütter, J. L. M. Rupp, L. J. Gauckler, *J. Power Sources* **2009**, *194*, 119–129.
- [128] G. Kresse, J. Furthmüller, *J. Phys. Rev. B* **1996**, *54*, 11169.
- [129] J. P. Pedew, K. Burke, M. Ernzerhof, *Phys. Rev. Lett.* **1996**, *77*.
- [130] P. E. Blöchl, *Phys. Rev. B* **1994**, *50*, 17953.
- [131] M. Nolan, S. Grigoleit, D. S. P. Sayle, G. Watson, *Surf. Sci.* **2005**, *576*, 217.
- [132] G. Henkelman, B. P. Uberuaga, H. Jonsson, *J. Chem. Phys.* **2000**, *113*, 9901.
- [133] R. D. Shannon, *Acta Crystallogr. A* **1976**, *31*, 751.